Flexible Electrodes Hot Paper

Deutsche Ausgabe: DOI: 10.1002/ange.201411125
Internationale Ausgabe: DOI: 10.1002/anie.201411125

Phosphorus-Doped Graphitic Carbon Nitrides Grown In Situ on Carbon-Fiber Paper: Flexible and Reversible Oxygen Electrodes**

*Tian Yi Ma, Jingrun Ran, Sheng Dai, Mietek Jaroniec, and Shi Zhang Qiao**

Abstract: *Flexible non-metal oxygen electrodes fabricated from phosphorus-doped graphitic carbon nitride nano-flowers directly grown on carbon-fiber paper exhibit high activity and stability in reversibly catalyzing oxygen reduction and evolution reactions, which is a result of N, P dual action, enhanced mass/charge transfer, and high active surface area. The performance is comparable to that of the state-of-the-art transition-metal, noble-metal, and non-metal catalysts. Remarkably, the flexible nature of these oxygen electrodes allows their use in folded and rolled-up forms, and directly as cathodes in Zn–air batteries, featuring low charge/discharge overpotential and long lifetime.*

Flexible energy-conversion and energy-storage systems attract increasing attention because of their unique features, such as shape conformability, light weight, small unit, which enable their applications in foldable, bendable, portable and even wearable devices.[1] However, the heavy, rigid and bulky configuration of oxygen electrodes in the current key renewable energy systems such as metal–air batteries, solar water-splitting devices, and fuel cells means they lag far behind the requirement of flexibility.[2] The design of flexible electrodes usually requires materials with three-dimensional (3D) architectures featuring excellent catalytic activity and good mechanical properties.[3] Recently, carbon-fiber paper (CFP), a soft current collector with a 3D porous network, high electron conductivity, and robust mechanical stability, has been employed as the replacement of conventional flat metal substrates (e.g. metallic foils, foams and meshes); integrating CFP with functional materials, such as metal oxides, phosphides, selenides and graphenes, is feasible.[4] Although considerable progress has been made to develop CFP-based electrodes for lithium-ion batteries and supercapacitors,[1a,b] there is still an enormous need for research on directly growing non-metal catalytically active species on CFP to fabricate flexible oxygen electrodes for oxygen reduction and evolution reactions.

[*] Dr. T. Y. Ma, J. R. Ran, Prof. S. Dai, Prof. S. Z. Qiao
School of Chemical Engineering
The University of Adelaide
Adelaide, SA 5005 (Australia)
E-mail: s.qiao@adelaide.edu.au
Prof. M. Jaroniec
Department of Chemistry and Biochemistry
Kent State University, Kent, OH 44240 (USA)

[**] This work is financially supported by the Australian Research Council (ARC) through the Discovery Project programs (DP140104062 and DP130104459).

Supporting information for this article is available on the WWW under http://dx.doi.org/10.1002/anie.201411125.

Oxygen reduction reaction (ORR) and oxygen evolution reaction (OER) are at the heart of rechargeable metal–air batteries and regenerative fuel cells.[2a,3b] Noble metals[5] and transition-metal oxides[6] are commonly utilized as the catalysts. However, high cost, scarcity, and inferior durability of noble metals, and complicated fabrication of transition-metal oxides with low conductivity largely prevent their practical applications. In contrast, non-metal materials consisting of earth-abundant elements (C, H, O, and N) that act as catalytically active components have been recently recognized as a new class of low-cost and environmentally benign electrocatalysts.[7–9] Among them, graphitic carbon nitrides (g-C_3N_4) with ultrahigh N content (theoretically up to 60 wt.%), stable and tailorable structure have been developed as efficient ORR[8] and OER[9] electrocatalysts. Nevertheless, it is still urgent to further improve the activity of g-C_3N_4-based catalysts that are anticipated to outperform metal-containing ones. Doping g-C_3N_4 is a promising route, which is stimulated by the fact that enhanced catalytic behavior (e.g. in photocatalysis) has been discovered by doping g-C_3N_4 with heteroatoms, such as B,[10a] P,[10b] S,[10c] and I[10d] to alter its electronic and textural properties. However, heteroatom-doped g-C_3N_4 has scarcely been employed for oxygen electrochemistry.

Herein phosphorus-doped g-C_3N_4 (P-g-C_3N_4) directly grown on CFP (PCN–CFP) is designed as a flexible oxygen electrode, which represents the first g-C_3N_4-based non-metal ORR/OER bifunctional electrocatalyst. The flower-like P-g-C_3N_4 composed of thin nanosheets is strongly coupled with CFP, giving a 3D hybrid network with high N content and substantial P doping, which lead to excellent ORR and OER activity and durability, superior to its P-free counterpart (CN–CFP), even comparable to Pt supported on CFP (Pt–CFP).

The fabrication of PCN–CFP is shown in Scheme 1. Commercial CFP was first mildly oxidized, creating abundant functional groups (e.g. -COO^-) on the surface to enhance its interaction with basic melamine as the N source. Ethylene diphosphonic acid was utilized as the P source, because of its acid–base interaction with melamine that can facilitate cross-linking. After N and P sources assembled on CFP surface in a hydrothermal process, they further condensed on the P-g-C_3N_4 under heating treatment in N_2 at 550 °C, affording PCN–CFP in different sizes and shapes for direct electrochemical usage. The high decomposition temperature of ethylene diphosphonic acid (over 400 °C, Figure S1 in Supporting Information), means that it is thermally stable until polycondensation of melamine starts, allows substantial and homogeneous P doping.

Large electrodes, for example, a 10×15 cm^2 sized PCN–CFP with a highly flexible shape (Figure 1a inset), can be

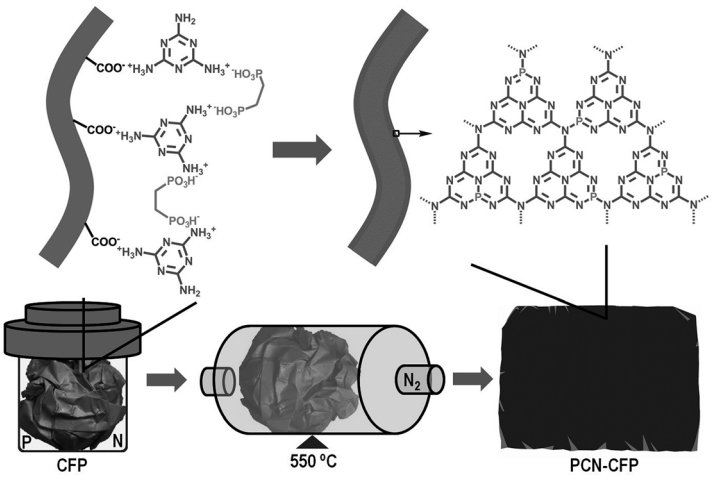

Scheme 1. Fabrication of P-g-C_3N_4 nanostructures directly grown on CFP.

through the involvement of heteroatom motifs (i.e. ethylene diphosphonic acid) that interact with melamine and in situ alter its polymerization route;[11] and the introduction of P (larger than C and N) can disturb the graphitic structure of g-C_3N_4, similar to the reported heteroatom-mediated "bottom-up" synthesis of g-C_3N_4 nanosheets.[11] In contrast, only bulky g-C_3N_4 particles are found on the surface of P-free CN-CFP (Figure S4). Furthermore, the energy dispersive X-ray spectroscopy (EDS) elemental mapping images of PCN-CFP (Figure S3) confirm the uniform dispersion of N, P, and C, indicating a homogeneous growth of P-g-C_3N_4 on CFP.

PCN–CFP is constructed by strong coupling of P-g-C_3N_4 and CFP, as evidenced by X-ray photoelectron spectra (XPS). The N 1s spectrum of PCN–CFP (Figure 2a), distinct from that of pure P-g-C_3N_4 (Figure S5), was deconvoluted into three components. The

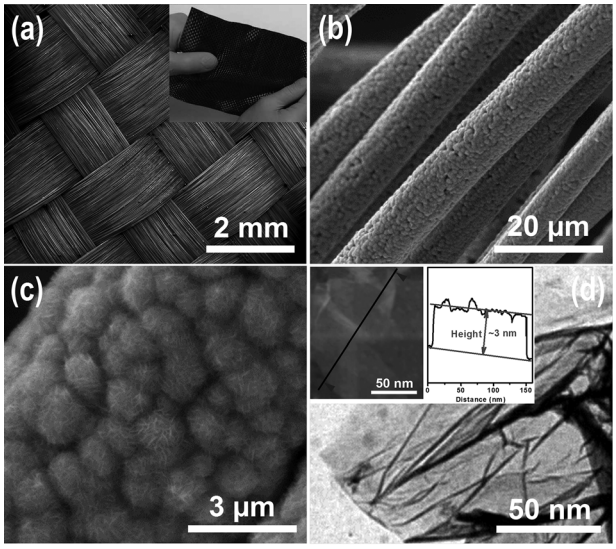

Figure 1. a–c) SEM images (Inset in panel (a): photograph of PCN–CFP). d) TEM (Inset: AFM images with the corresponding height profile) of P-g-C_3N_4 nanosheets, collected from P-g-C_3N_4 nano-flowers in PCN–CFP.

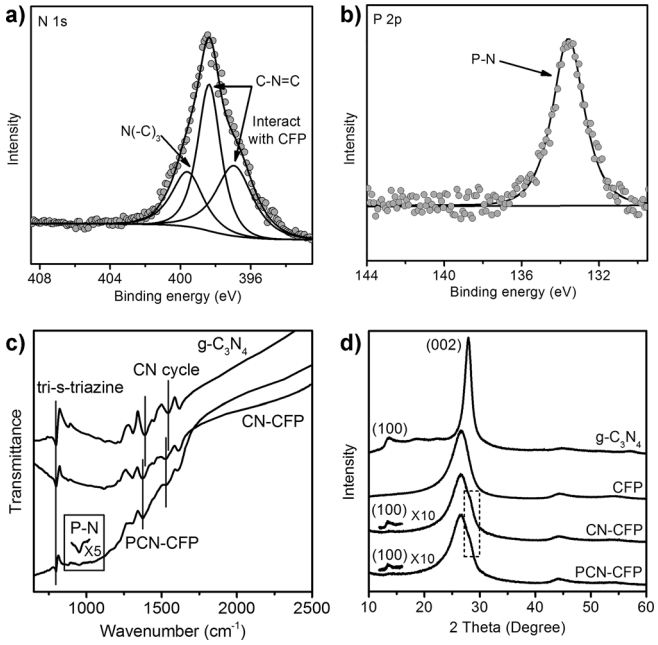

Figure 2. High-resolution XPS spectra of a) N1s and b) P2p core levels in PCN-CFP. c) FT-IR spectra and d) XRD patterns of the synthesized materials.

prepared by this method. Scanning electron microscopy (SEM) images (Figure 1a,b) indicate PCN–CFP maintains the fibrous morphology of CFP, which has a 3D network consisting of carbon fibers with a diameter of approximately 8 μm (Figure S2). The textured surface of carbon fibers and the acid–base interaction between -COOH on CFP, basic melamine, and ethylene diphosphonic acid (Scheme 1) facilitate adsorption of precursors and growth of the P-g-C_3N_4 nanostructure strongly bound to CFP.[4] The magnified SEM image (Figure 1c) shows that flower-like P-g-C_3N_4 densely grows on CFP creating a porous framework. Transmission electron microscopy (TEM, Figure 1d, S3) and atomic force microscopy (AFM, Figure 1d inset) reveals that the flower-like P-g-C_3N_4 nanostructure consists of interconnected nanosheets having thickness of approximately 3 nm (equal to ca. 9 CN atomic monolayers). The nanosheets are formed

peak at 399.5 eV is attributed to the bridging N atoms in N(-C)$_3$ or N bonded with H atoms, and the dominant peak at 398.4 eV corresponds to the sp^2-bonded N in triazine rings (C–N=C),[10] which splits to form an obvious new shoulder peak at 396.9 eV, caused by strong interaction between carbon fibers and N in g-C_3N_4.[9,12] The peak of P2p binding energy is centered at 133.6 eV, which is typical for P–N coordination,[13] indicating that P most probably replaces C in g-C_3N_4 to form P–N bonds (Figure 2b).[10b] The XPS survey spectrum and high-resolution spectra of the most common metals in carbon fibers (e.g. Ni, Co and Fe) indicate PCN–CFP contains only C, N, O, and P without detectable impurities on the surface (Figure S6), showing 13.2 wt% of N and 0.9 wt% of P.

The strong interaction between in situ grown P-g-C_3N_4 and CFP is also confirmed by Fourier transform infrared (FT-IR) spectra (Figure 2c), in which the characteristic stretching modes of CN heterocycles in PCN–CFP between 900 and 1700 cm^{-1}[10] show apparent shifts as compared to pure g-C_3N_4, for example, 1389→1373 cm^{-1} and 1543→1528 cm^{-1}. One new band at around 950 cm^{-1} is attributed to P–N stretching mode,[10b,13] implying a substantial P incorporation, consistent with the EDS and XPS results. The crystalline structure of g-C_3N_4 is well preserved in PCN–CFP, as evidenced by two typical signals on the X-ray diffraction (XRD) pattern (Figure 2d) including the shoulder peak at 27.5° (2θ) from CN graphitic-like layers and the low-angle peak at 13.3° from in-planar repeated tri-*s*-triazine units.[10]

PCN–CFP can be directly used as the working electrode for both ORR and OER (Figure S7, Video S1) without extra substrates or binders. As shown by linear sweep voltammograms (LSVs), the pristine CFP exhibits negligible activities, while PCN–CFP affords an onset potential of 0.94 V versus reversible hydrogen electrode (RHE), and a half-wave potential ($E_{1/2}$) of 0.67 V in the ORR region (Figure 3a),

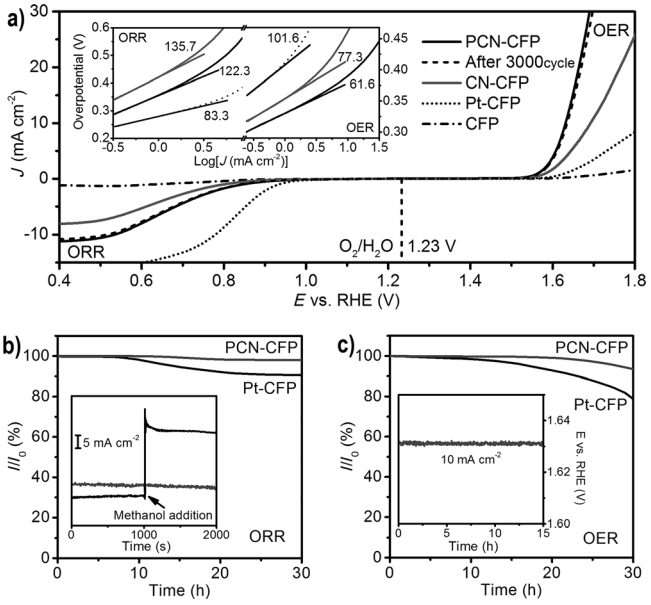

Figure 3. a) Linear-sweep voltammograms of PCN–CFP, CN–CFP, Pt–CFP, and CFP in O_2-saturated 0.1 M KOH solution at scan rate of 0.5 $mV s^{-1}$ (Inset: Tafel plots of PCN–CFP, CN–CFP, Pt–CFP). b) ORR chronoamperometric response of PCN–CFP and Pt–CFP at a constant potential of 0.40 V (Inset: ORR chronoamperometric response after methanol addition). c) OER chronoamperometric response of PCN–CFP and Pt–CFP at a constant potential of 1.63 V ($E_{j=10}$). Inset: OER chronopotentiometric response at a constant current density of 10.0 $mA cm^{-2}$.

which are closer to those of Pt–CFP (onset potential = 0.99 V, $E_{1/2}$ = 0.80 V) than those observed for the P-free counterpart CN–CFP (onset potential = 0.90 V, $E_{1/2}$ = 0.63 V). The more positive onset and half-wave potentials indicate a more facile ORR process initiated on PCN–CFP than that on CN–CFP. In OER region, PCN–CFP affords a sharp onset potential at 1.53 V, lower than that of CN–CFP at 1.55 V and Pt–CFP at 1.59 V (Figure 3a). The oxidation current of PCN–CFP largely surpasses those of CN–CFP and Pt–CFP; its operating potential to deliver a 10.0 $mA cm^{-2}$ current density ($E_{j=10}$), a critical metric related to solar fuel synthesis,[14] is 1.63 V, much lower than those of CN–CFP (1.69 V) and Pt–CFP (1.82 V).

The overall oxygen electrode activity and reversibility can be evaluated by the variance of the OER and ORR metrics ($\Delta E = E_{j=10} - E_{1/2}$).[5,6,14,15] The smaller the ΔE value is, the closer the catalyst is to an ideal reversible oxygen electrode. PCN–CFP exhibits a ΔE of 0.96 V, lower than that of CN–CFP (1.06 V) and Pt–CFP (1.02 V), also comparable to the highly active electrocatalysts including noble-metal (e.g. Pt/C,[15a] ΔE = 0.94 V; Ir/C,[15b] ΔE = 0.92 V), transition-metal (e.g. $CaMn_4O_x$,[15b] ΔE = 1.04 V; Ni_xO_y/N-doped C,[15a] ΔE = 0.93 V), and non-metal materials (e.g. N-doped graphene/carbon nanotube,[15c] ΔE = 1.00 V). A detailed comparison of various state-of-the-art bifunctional catalysts reported recently is presented in Table S1, further confirming the high catalytic activity and reversibility of PCN–CFP for ORR and OER.

PCN–CFP exhibits a Tafel slope value of 122.3 mV $decade^{-1}$ in ORR region (Figure 3a, inset), much lower than that of CN–CFP (135.7 mV $decade^{-1}$); while in OER region, the lowest Tafel slope value of PCN–CFP (61.6 mV $decade^{-1}$) largely outperforms other control groups (CN–CFP: 77.3 mV $decade^{-1}$, Pt–CFP: 101.6 mV $decade^{-1}$) and reported electrocatalysts (Table S1), suggesting its favorable reaction kinetics. Furthermore, by employing the rotating ring-disk electrode (RRDE) technique to investigate the reaction mechanism (Figure S8), the reversible ORR/OER process occurring on PCN–CFP is dominated by a desirable four-electron pathway with negligible formation of peroxide intermediates, that is, $4OH^- \leftrightarrow O_2 + 2H_2O + 4e^-$. And the observed oxidation current can be fully attributed to OER with a high Faradaic efficiency of 98.7%.

PCN–CFP shows a strong durability as revealed by the chronoamperometric response (Figure 3b), retaining 97.8% of the initial ORR current even after 30 h, whereas Pt–CFP loses much more (9.6%) of its initial current, indicating the apparent advantage in long-term stability of non-metal PCN–CFP over noble metals. A distinct methanol oxidation reaction occurs after methanol introduction in the case of Pt–CFP (Figure 3b, inset), but the current density of PCN–CFP shows no obvious change, indicating its high selectivity to ORR with strong methanol tolerance. Moreover, PCN–CFP exhibits a slight OER current attenuation of 6.6% after 30 h (Figure 3c) with no phase change or leaching of the active species (Figure S9), whereas Pt–CFP displays a 3.2 times larger current attenuation of 21.2%. PCN–CFP can also afford a nearly constant operating potential at 1.63 V ($E_{j=10}$) to deliver a 10.0 $mA cm^{-2}$ current density in 15 h (Figure 3c, inset). Even at a high operating potential of 1.70 V (delivering a large current density of ~35 $mA cm^{-2}$), no peeling of the catalysts is observed (Video S1). Further, PCN–CFP is highly stable and can withstand accelerated degradation with a scanning rate of 100 $mV s^{-1}$ for 3000 cycles (dash line in Figure 3a), this stability is a result of the strong coupling between P-g-C_3N_4 and CFP.

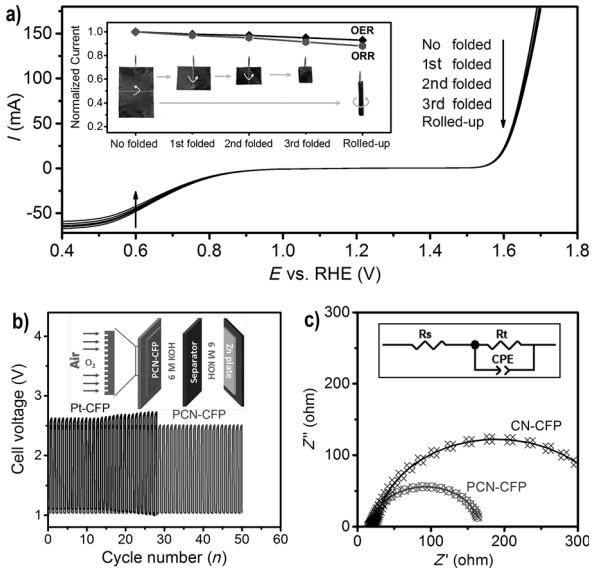

Figure 4. a) LSVs currents of PCN–CFP in different folded and rolled-up forms. The currents of the original unfolded electrode are normalized to 1. Inset: variations of the ORR (at 0.40 V) and OER (at 1.63 V). b) Charge-discharge cycling curves using PCN–CFP and Pt–CFP directly as the air cathodes (Inset: schematic configuration of Zn–air batteries). c) EIS (recorded at 1.60 V) of PCN-CFP and CN-CFP (Inset: the equivalent circuit diagram).

To see if PCN–CFP fulfills the flexibility demands, its performance was measured in different folded and rolled-up forms (Figure 4a, Video S1). Even after folding the PCN–CFP electrode three times, 91.3% of the initial ORR current and 94.6% of the initial OER current were maintained; and the LSV of the folded PCN–CFP after 3000 potential cycles exhibits negligible current loss and morphology change (Figure S10), indicating the high cyclic stability of PCN–CFP even in folded forms. The highly rolled-up PCN–CFP is capable of preserving 87.8% of the initial ORR current and 92.7% of the initial OER current, consistent with the smooth O_2 bubble generation in different electrode forms observed in Video S1. The aforementioned facts reveal that PCN–CFP possesses high physical flexibility, stability, and mechanical integrity towards folding and rolling-up treatments.

To demonstrate its feasibility in real energy devices, a Zn–air battery was constructed by directly using PCN–CFP as the air cathode (Figure 4b, inset). As shown by the polarization curves for the assembled Zn–air battery (Figure S11), PCN–CFP affords a current density of 20 mA cm^{-2} at 1.05 V during discharging and at 2.46 V during charging, outperforming that of Pt–CFP (2.63 V during charging), which is consistent with LSVs obtained in the three-electrode system. More importantly, no obvious potential change is observed when PCN–CFP is used as the air cathode for over 50 charge–discharge cycles, whereas an apparent increase in both charge and discharge overpotentials is observed after 15 cycles for Pt–CFP (Figure 4b). Therefore, the bifunctional PCN–CFP electrode is feasible in practical metal–air batteries, capable of reducing charging overpotential and enhancing cyclic stability.

Besides the N-induced positively charged C atoms that are commonly considered as the active centers for both ORR and OER,[7–9] P species are also critical in promoting the electroactivity. When P is doped into g-C_3N_4, three of its five valence-electrons form covalent bonds with the N neighbors (P–N bonds confirmed by XPS and FT-IR) to adopt a forced planar structure (Scheme 1), and the remaining lone pair can delocalize to the π-conjugated tri-*s*-triazine of P-g-C_3N_4, leaving partially positively charged P^+ centers,[10b] which act as the reinforcing active sites. New redox signals arising from P^+ are visible on the differential pulse voltammograms (DPVs, Figure S12a) and cyclic voltammograms (CVs, Figure S12b) of PCN–CFP. Moreover, the heteroatom (e.g. P) doping can adjust electronic structure and enhance the delocalized π bonds of g-C_3N_4,[10,11] consequently improving the conductivity and charge transfer. Accordingly, the semicircular diameter in the electrochemical impedance spectrum (EIS) of PCN–CFP is much smaller than that of CN–CFP (Figure 4c, S13), owing to a smaller contact and charge-transfer impedance.

Furthermore, the strong coupling between P-g-C_3N_4 and CFP facilitates the electron transfer between the two components,[8,9] and the 3D nanostructure of PCN–CFP favors the smooth transport of reactants and products (e.g. O_2, Video S1). More importantly, PCN–CFP has a large catalytically active surface area, which was evaluated by the electrochemical double-layer capacitance (C_{dl}, Figure S14). C_{dl} of PCN–CFP is confirmed to be 21.3 mF cm^{-2}, which is much higher than that of CN–CFP (C_{dl} = 1.6 mF cm^{-2}). Since C_{dl} is proportional to the active surface area of electrocatalysts,[4] the results demonstrate the formation of P-g-C_3N_4 nano-flowers induced by P doping is more effective in enlarging the active surface area than pure g-C_3N_4 bulky particles.

In summary, P-g-C_3N_4 consisting of thin nanosheets directly grown on CFP performs as a 3D foldable and rollable oxygen electrode. The outstanding activity, stability, and reversibility of PCN–CFP for ORR and OER allow its direct use as the air cathode in Zn–air batteries featuring low overpotential and long lifetime. This work will pave the way to a large variety of flexible electrodes constructed from non-metal polymeric and carbonaceous materials promoted by heteroatoms such as N, S, P, and B.

Keywords: graphitic carbon nitride · nanostructure · oxygen evolution · oxygen reduction · phosphorus doping

How to cite: *Angew. Chem. Int. Ed.* **2015**, *54*, 4646–4650
Angew. Chem. **2015**, *127*, 4729–4733

[1] a) X. Wang, X. Lu, B. Liu, D. Chen, Y. Tong, G. Shen, *Adv. Mater.* **2014**, *26*, 4763–4782; b) L. Li, Z. Wu, S. Yuan, X. B. Zhang, *Energy Environ. Sci.* **2014**, *7*, 2101–2122; c) W. Zeng, L. Shu, Q. Li, S. Chen, F. Wang, X. M. Tao, *Adv. Mater.* **2014**, *26*, 5310–5336.

[2] a) Z. Q. Peng, S. A. Freunberger, Y. H. Chen, P. G. Bruce, *Science* **2012**, *337*, 563–566; b) T. W. Kim, K. S. Choi, *Science* **2014**, *343*, 990–994.

[3] a) P. Zhang, J. Zhang, J. Gong, *Chem. Soc. Rev.* **2014**, *43*, 4395 – 4422; b) F. Y. Cheng, J. Chen, *Chem. Soc. Rev.* **2012**, *41*, 2172 – 2192.
[4] a) D. Kong, H. Wang, Z. Lu, Y. Cui, *J. Am. Chem. Soc.* **2014**, *136*, 4897 – 4900; b) J. Q. Tian, Q. Liu, A. M. Asiri, X. P. Sun, *J. Am. Chem. Soc.* **2014**, *136*, 7587 – 7590; c) L. Liu, Z. Niu, L. Zhang, W. Zhou, X. Chen, S. Xie, *Adv. Mater.* **2014**, *26*, 4855 – 4862; d) L. Shen, Q. Che, H. Li, X. Zhang, *Adv. Funct. Mater.* **2014**, *24*, 2630 – 2637.
[5] a) X. P. Han, F. Y. Cheng, Y. R. Zhang, J. G. Yang, Y. X. Hu, J. Chen, *Adv. Mater.* **2014**, *26*, 2047 – 2051; b) H. Over, *Chem. Rev.* **2012**, *112*, 3356 – 3426.
[6] a) J. I. Jung, H. Y. Jeong, J. S. Lee, M. G. Kim, J. Cho, *Angew. Chem. Int. Ed.* **2014**, *53*, 4582 – 4586; *Angew. Chem.* **2014**, *126*, 4670 – 4674; b) F. Y. Cheng, J. Shen, B. Peng, Y. D. Pan, Z. L. Tao, J. Chen, *Nat. Chem.* **2011**, *3*, 79 – 84.
[7] a) D. W. Wang, D. S. Su, *Energy Environ. Sci.* **2014**, *7*, 576 – 591; b) Y. Zhao, R. Nakamura, K. Kamiya, S. Nakanishi, K. Hashimoto, *Nat. Commun.* **2013**, *4*, 2390.
[8] a) J. Liang, Y. Zheng, J. Chen, J. Liu, D. Hulicova-Jurcakova, M. Jaroniec, S. Z. Qiao, *Angew. Chem. Int. Ed.* **2012**, *51*, 3892 – 3896; *Angew. Chem.* **2012**, *124*, 3958 – 3962; b) S. Yang, X. Feng, X. Wang, K. Müllen, *Angew. Chem. Int. Ed.* **2011**, *50*, 5339 – 5343; *Angew. Chem.* **2011**, *123*, 5451 – 5455.
[9] a) T. Y. Ma, S. Dai, M. Jaroniec, S. Z. Qiao, *Angew. Chem. Int. Ed.* **2014**, *53*, 7281 – 7285; *Angew. Chem.* **2014**, *126*, 7409 – 7413; b) J. Q. Tian, Q. Liu, A. M. Asiri, K. A. Alamry, X. P. Sun, *ChemSusChem* **2014**, *7*, 2125 – 2132.
[10] a) S. C. Yan, Z. S. Li, Z. G. Zou, *Langmuir* **2010**, *26*, 3894 – 3901; b) Y. Zhang, T. Mori, J. Ye, M. Antonietti, *J. Am. Chem. Soc.* **2010**, *132*, 6294 – 6295; c) G. Liu, P. Niu, C. Sun, S. C. Smith, Z. Chen, G. Q. Lu, H. M. Cheng, *J. Am. Chem. Soc.* **2010**, *132*, 11642 – 11648; d) G. Zhang, M. Zhang, X. Ye, X. Qiu, S. Lin, X. Wang, *Adv. Mater.* **2014**, *26*, 805 – 809.
[11] Z. Lin, X. Wang, *Angew. Chem. Int. Ed.* **2013**, *52*, 1735 – 1738; *Angew. Chem.* **2013**, *125*, 1779 – 1782.
[12] Q. Liu, J. Zhang, *Langmuir* **2013**, *29*, 3821 – 3828.
[13] H. Gu, Y. Gu, Z. Li, Y. Ying, Y. Qian, *J. Mater. Res.* **2003**, *18*, 2359 – 2363.
[14] C. C. L. McCrory, S. Jung, J. C. Peters, T. F. Jaramillo, *J. Am. Chem. Soc.* **2013**, *135*, 16977 – 16987.
[15] a) J. Masa, W. Xia, I. Sinev, A. Zhao, Z. Sun, S. Grützke, P. Weide, M. Muhler, W. Schuhmann, *Angew. Chem. Int. Ed.* **2014**, *53*, 8508 – 8512; *Angew. Chem.* **2014**, *126*, 8648 – 8652; b) Y. Gorlin, T. F. Jaramillo, *J. Am. Chem. Soc.* **2010**, *132*, 13612 – 13614; c) G. L. Tian, M. Q. Zhao, D. Yu, X. Y. Kong, J. Q. Huang, Q. Zhang, F. Wei, *Small* **2014**, *10*, 2251 – 2259.

Received: November 20, 2014
Published online: December 17, 2014

